



A Novel Methodology for the Thermographic Cooling Rate Measurement during Powder Bed Fusion of Metals Using a Laser Beam

David L. Wenzler^{1,2} · Katharina Bergmeier^{1,2} · Siegfried Baehr^{1,2} · Johannes Diller^{3,4} · Michael F. Zaeh^{1,2}

Received: 22 November 2022 / Accepted: 3 January 2023 / Published online: 23 January 2023
© The Author(s) 2023

Abstract

Powder bed fusion of metals using a laser beam (PBF-LB/M) is a process that enables the fabrication of geometrically complex parts. In this process, a laser beam melts a metallic powder locally to build the desired geometry. The melt pool solidifies rapidly, which results in high cooling rates. These rates vary during the process in line with the geometric characteristics of the part, which leads to a non-uniform microstructure along with anisotropic mechanical properties. The unknown part characteristics prevent the process from being used in safety-critical applications. Thermographic in situ process monitoring provides information about the thermal field, enabling predictions of the resulting material properties. This study presents a novel methodology for the thermographic measurement of cooling rates during the PBF-LB/M process using a high-speed thermographic camera. The cooling rates occurring during the manufacturing of 316L tower-like specimens were measured. The cooling rate decreased with increasing build height, due to the heat accumulation in the parts. The microhardness profile of the parts was tested perpendicularly and parallel to the build direction. A significant decrease in hardness values was observed along the build height. The measured cooling rate was correlated to the microhardness profile of the specimens using a Hall–Petch type relationship. The results show a high level of reproducibility of the cooling rates between different specimens in the same build job as well as between subsequent build jobs. The presented methodology allows studying the effects of the geometry on the cooling rates and the resulting mechanical properties of 316L specimens.

Keywords Additive manufacturing (AM) · Laser powder bed fusion (LPBF) · Process monitoring · Stainless steel 316L · Thermal history

✉ David L. Wenzler
david.wenzler@tum.de

Katharina Bergmeier
katharina.bergmeier@tum.de

Siegfried Baehr
siegfried.baehr@tum.de

Johannes Diller
johannes.diller@tum.de

Michael F. Zaeh
michael.zaeh@tum.de

¹ Technical University of Munich, Munich, Germany

² TUM School of Engineering and Design, Institute for Machine Tools and Industrial Management (iwb), Boltzmannstrasse 15, 85748 Garching, Bavaria, Germany

³ Technical University of Munich, Munich, Germany

⁴ TUM School of Engineering and Design, Chair of Metal Structures, Arcisstrasse 21, 80333 Munich, Bavaria, Germany

Introduction

Powder bed fusion of metals using a laser beam (PBF-LB/M) is an additive manufacturing process in which a laser selectively melts a metallic powder. The PBF-LB/M process offers a high degree of design freedom and enables the manufacturing of lightweight components, such as shape-optimized connection nodes for construction applications [1]. Where safety is paramount, knowledge of the mechanical properties of the parts is crucial. However, these can be complicated to determine, as they depend on the thermal history of the process, which is highly dynamic [2]. In the PBF-LB/M process, the melt solidifies at high cooling rates resulting in stainless steel 316L with a fine-cellular microstructure [3]. The fine sub-grain structure enhances the strength of the additively manufactured material compared to conventional material [3]. Varying the cooling rate can cause changes to both the microstructure and the mechanical properties of components with different geometries [4].

Knowledge of the local cooling rate during the build would make it possible to predict the local part properties [5].

Bertoli et al. [6] used a high-speed camera to monitor the fabrication of 316L single tracks with different process parameters and calculated the average cooling rates from the resulting video data. The authors extracted the time interval between the frames when the laser focused on a fixed position and when the melt solidified at this position. The cooling rate was calculated by this interval and a fixed temperature range between the boiling point and the solidification point of the material. The cooling rates reported were between 1×10^6 K/s and 7×10^6 K/s.

In contrast to individual melt paths, the transient thermal field during the PBF-LB/M process is dominated by the heating and cooling cycles of adjacent laser tracks, leading to varying cooling rates.

Evans et al. [7] used the semi-analytical temperature model of the PBF-LB/M process proposed by Plotowski et al. [8] to estimate the cooling rate. They compared the results of single- and multi-track scan patterns. The authors found that the cooling rate was nearly constant in single tracks but varied along the paths of multi-track scan patterns. The cooling rate decreased at the turning points of the laser and was higher for longer scan paths. Hooper [9] used an in-axis process-monitoring setup based on two high-speed cameras to measure the temperatures around the melt pool. This two-wavelength setup captured the thermal field within the melt pool and the authors extracted the cooling rate with a high spatial and temporal resolution. The large quantity of data limited the acquisition time to a few seconds, with the result that it was not possible to measure complete layers.

Heigel and Lane [10] employed an off-axis thermographic setup to measure the cooling rates of several layers during the manufacturing of a complex benchmark part. The thermographic camera captured an area of approximately $12 \text{ mm} \times 6 \text{ mm}$ with a spatial resolution of $360 \text{ pixels} \times 126 \text{ pixels}$. The camera measurements were corrected for the solidification temperature by identifying the solidification discontinuity. The cooling rate was calculated using a fixed temperature interval between the solidification temperature and an arbitrarily chosen lower temperature value. Cooling rates of between 1×10^5 K/s and 7×10^5 K/s were reported. The authors found that cooling rates in complex parts are influenced by the scanning strategy and geometrical differences.

To sum up, there are only limited studies that consider the cooling rate measurement during the PBF-LB/M process. The current literature does not give a uniform definition of the cooling rate. As a result, it is calculated on the basis of a variety of temperature intervals, making their results difficult to compare. Existing methods are only able to measure a small area of the build platform. Hence, it is not possible to compare the cooling rates of different parts or different

sections of large parts. This study presents a novel methodology for the thermographic measurement of cooling rates during the PBF-LB/M process. Cooling rates were measured from the slope of the cooling curve at the solidification temperature. In contrast to current approaches, no arbitrarily chosen temperature interval was used in the calculations. The experiments had a large thermographic field of view. To show the reproducibility of the cooling rate measurements, several specimens were built. The cooling rates were correlated to spatial changes in the mechanical properties of the manufactured test specimens. This study was conducted with 316L stainless steel due to the well-understood relationship between the cooling rate and the microstructure.

Cooling Rate Measurement Methodology

The objectives of the methodology presented in this work were to measure the solidification cooling rate during the manufacturing of large-scale components and to compare the results of several parts on the build platform. This necessitated monitoring a wide area of the build platform. The spatial resolution per pixel scales with the area of interest. A setup with a large field of view cannot resolve a small PBF-LB/M melt pool. The size of the melt pool is in the order of a few hundred μm [11]. Measuring the temperature of a small area that is not resolved by multiple pixels results in a high level of uncertainty [12]. To address this, a five-step methodology for measuring cooling rates is proposed (see Fig. 1).

This methodology employs a statistical data analysis to ensure the reliability of the measurements. In the first step of applying this methodology, the signal value of the solidification temperature was detected for each layer. This information was used to calculate the apparent emissivity at this temperature and to perform a single-point correction of the data. The cooling cycle after the solidification of each pixel was extracted from the corrected data. The cooling curve was obtained by fitting the extracted data to a simplified analytical temperature model. In the final step, the solidification cooling rate was calculated from the first-order derivative of the fitted cooling curve. The following subsections describe these five steps in more detail.

Solidification Point Detection

The first step of the cooling rate measurement process is to detect the solidification point. The cooling curve in the PBF-LB/M process shows an almost exponential progression [13]. Hence, the cooling rate is very sensitive to the temperature value at which it is calculated. To calculate the solidification cooling rate accurately, the solidification temperature signal value must be determined. Due to the latent heat of fusion, the cooling curve shows a discontinuity at

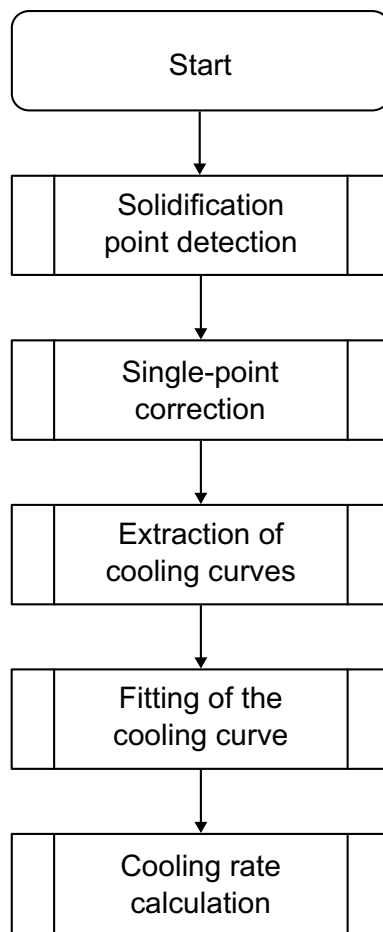


Fig. 1 Five-step methodology for the thermographic cooling rate measurement

the liquid to solid transition. This discontinuity is marked by the first minimum of the second-order derivative of the cooling curve [14]. The camera value at the discontinuity corresponds to the solidification temperature. To identify the discontinuity in the camera signal of a pixel, it must lie directly in the laser path. As a result, only a limited number of pixels are available to identify the solidification discontinuity. A multi-stage procedure was applied to account for measurement uncertainties due to the experimental setup.

First, the maximum values were calculated for each pixel in a layer. The pixels passed directly by the laser have the highest measured values of all pixels in that layer. Therefore, only pixels with values close to the maximum of the thermographic camera were used to detect the solidification point. The acceptable range depends on the thermographic setup and is determined empirically. In this study, the digital dynamic range of the thermographic camera was 14-bit = 16,384 counts, and the threshold was set to 1.3×10^4 counts. The temperature curve of these pixels after interacting with the laser was extracted for further analysis. Next, the second-order derivative of the cooling curve for these pixels was approximated by the

second-order central difference algorithm. The first minimum of the second-order derivative was determined to identify the time of the solidification transition. If no clear minimum was detected, the values were discarded. A normal distribution of the calculated solidification points was expected due to the measurement uncertainties of the thermographic setup. Therefore, the median value of each layer was used as the solidification temperature. The surrounding temperature of a pixel increases as a consequence of the heat accumulation during the build of the part. This creates an offset in the thermographic signal [12]. To account for this effect, the solidification temperature was calculated for each layer.

Single-point Correction

The thermographic camera measures the intensity of the infrared radiance that the surface of the part emits according to its temperature. The relationship between the temperature T of an ideal black body and its spectral radiance $L_{\lambda\text{Bb}}$ is described by Planck's law as

$$L_{\lambda\text{Bb}}(\lambda, T) = \frac{2 \cdot h \cdot c^2}{\lambda^5} \frac{1}{e^{\left(\frac{h \cdot c}{\lambda \cdot k_{\text{B}} \cdot T}\right)} - 1}. \quad (1)$$

Here, h is the Planck constant, c is the speed of light, λ is the wavelength, and k_{B} is the Boltzmann constant. Real bodies emit less radiation than a black body at the same temperature. The ratio between the two radiations is described by the emissivity ϵ , which depends on the material, the surface conditions, and the temperature of the target object [15]. The emissivity is also dependent on the wavelength and is affected by the viewing angle [16]. The signal level is further reduced by losses due to the optical elements in the measurement path. The transmissivity of the optical path can be expressed as τ_{optics} where $\tau_{\text{optics}} < 1$. The apparent emissivity takes these losses into account by $\epsilon_{\text{app}} = \epsilon_{\text{surface}} \cdot \tau_{\text{optics}}$. It is therefore lower than the actual emissivity of the material. The apparent emissivity needs to be determined for the specific measuring task to enable conclusions to be made about the absolute temperature. The focus of this work is on the cooling rates starting at the solidification temperature. An absolute temperature calibration of the entire temperature range was beyond the scope of the study. The thermographic data were corrected using the single-point correction method. Here, the apparent emissivity is determined for a single temperature value and assumed to be constant over the measured temperature range. Deviations from this assumption could influence the progress of the measured cooling curve. This error was considered to be small since the cooling rate was determined at the detected solidification temperature T_s . Single-point correction requires a pair of correlating temperatures. Here, these are the solidification temperature ($T_{s,\text{true}}$ of 316L) of 1663.15 K and the apparent

temperature corresponding to the solidification signal $T_{s,app}$ obtained in the previous step. The solidification signal was converted into an apparent temperature using the black body calibration curve of the camera. Using this temperature couple, the apparent emissivity at the solidification temperature $\epsilon_{app}(T_s)$ was calculated by

$$\epsilon_{app}(T_s) = \frac{\int_{\lambda_1}^{\lambda_2} L_{\lambda TC}(\lambda, T_{s,app}) d\lambda}{\int_{\lambda_1}^{\lambda_2} L_{\lambda Bb}(\lambda, T_{s,true}) d\lambda} \quad (2)$$

In Eq. (2), λ_1 and λ_2 are the limits of the spectral range of the camera, and $L_{\lambda TC}$ and $L_{\lambda Bb}$ are the spectral radiance values for $T_{s,app}$ and $T_{s,true}$ calculated by Eq. (1).

The apparent emissivity calculated by Eq. (2) neglects the spectral responsivity of the thermographic camera sensor $r(\lambda)$. If $r(\lambda)$ shows a high dependency on the wavelength, $r(\lambda)$ must be included in Eq. (2). The thermographic camera sensor used in this study had a $r(\lambda) > 80\%$ within its spectral range. Thus, $r(\lambda)$ was neglected. The apparent temperature values obtained from the thermographic camera were corrected using ϵ_{app} and a numerical solution of the integrals in Eq. (2).

Extraction of the Cooling Curve

In the PBF-LB/M process, the material is subjected to multiple heating and cooling cycles. In an individual layer, these thermal cycles are caused by the hatching of the laser. The cooling rate was calculated for the last of these heating and cooling cycles, where the solidification time was exceeded. The material is also re-molten in the build direction, as the penetration depth usually includes multiple layers [17]. This creates an offset between the measured cooling rates and the solidified microstructure. However, the layer thickness in the PBF-LB/M process is in the range of tens of microns [18]. Since the measurements in this work were focused on the macroscopic process-property relationship, this offset was neglected.

Fitting of the Cooling Curve

To calculate the cooling rate, the extracted thermographic data were fitted using the analytical temperature model of the PBF-LB/M process proposed by [19]. In contrast to a piecewise interpolation of the measured data, the fit of the analytical model includes all data points of the cooling curves. It is thus more robust against signal deviations due to measurement errors. The fitted model provides a continuous, physically interpretable curve for evaluating the cooling rate. The temperature after solidification is approximated for a semi-infinite bar with a constant temperature T_0 and a higher temperature T_1 in the topmost layers at the current build height z_n . It is

assumed that heat is solely transported by conduction. Temperature-dependent material properties and phase transitions are neglected. The heat is inserted homogeneously into the volume fraction at the top layer of the bar. With these simplifications, the cooling temperature profile after the solidification can be approximated by [19]

$$T(z_n = 0, t) \approx T_0 + n \cdot \frac{\eta \cdot P}{v \cdot d \cdot c_p \cdot \rho \cdot \sqrt{\pi \cdot a}} \frac{1}{\sqrt{t}} \quad (3)$$

In Eq. (3), η is the absorption coefficient, P is the laser power, v is the scan velocity, d is the hatch distance, c_p is the specific heat capacity, ρ is the material density, a is the thermal diffusivity, and n is the hatch factor. The hatch factor n considers the dependency of the energy input on the length of the laser tracks.

The maximum value of the extracted cooling curve was shifted to $t = 0$ s. The temporal delay between the heat input and the first measurement value varies in relation to the frame rate of the thermographic camera. A time offset t_0 was introduced into Eq. (3) to take this delay into account. The MATLAB[®] curve fitting toolbox was used for the curve fitting. The fitting parameters and their initial values were $T_0 = 400$ K, $n = 1$, and $t_0 = 0.001$ s. A lower limit was set for the parameters of $T_0 = 273$ K, $n = 0$, and $t_0 = 0$ s. The fitting results were evaluated by the coefficient of determination R^2 . Results with a value of $R^2 < 0.95$ were rejected. The threshold was chosen in reference to the 95 % confidence interval.

Cooling Rate Calculation

In this study, the solidification cooling rate $\dot{T}(t_s)$ is defined as the slope of the cooling curve at the solidification temperature or at the time of solidification t_s . According to this definition, the cooling rate is calculated by

$$\dot{T}(t_s) = \frac{dT(t_s)}{dt} \quad (4)$$

Using Eq. (3), the cooling rate can be calculated as

$$\dot{T}(t_s) = -\frac{1}{2} \cdot n \cdot \frac{\eta \cdot P}{v \cdot d \cdot c_p \cdot \rho \cdot \sqrt{\pi \cdot a}} \cdot t_s^{-\frac{3}{2}} \quad (5)$$

Using the fitting parameters and the solidification temperature T_s , t_s can be calculated by Eq. (3) for each temperature curve.

Materials and Post-process Analysis

The proposed methodology was tested by experimental investigation. The aim of the experiments was to trigger a variation in the cooling rate by causing heat to accumulate

in the specimens due to a short inter-layer time (ILT) of approximately 14 s. To demonstrate the reproducibility of the methodology, a total of four identical 316L test specimens were built in two separate build jobs. The setup used for manufacturing and for monitoring the process is described in the following.

Thermographic Setup

The experiments were performed on an EOSINT M280 machine (EOS, Krailling, Germany). The machine is equipped with a 400 W fiber laser with a beam diameter of 100 μm . A Flir xc6901sc thermographic camera (FLIR Systems, Wilsonville, OR, USA) was used to measure the thermal field during the PBF-LB/M process. Fig. 2 illustrates the thermographic setup. The camera sensitivity covered a spectral range of 2 μm to 5 μm . The 50 mm lens was complemented by an internal neutral density (ND) filter with a transmittance of 10%. The purpose of the ND filter was to reduce the incoming radiation and prevent the camera sensor from saturating when measuring higher temperature ranges.

The camera was mounted on an aluminum frame outside of the process chamber. The camera was positioned at a working distance of 500 mm by means of a slider mount. The viewing angle was 14° to the Z axis and -5° to the X axis. Stoppers in the aluminum frame allowed the camera position to be reproduced in the various experiments.

The optical access to the chamber was through a germanium long-pass filter window (Edmund Optics, Nether

Poppleton, North Yorkshire, UK). The filter had a diameter of 50 mm and a transmission of $> 85\%$ in the spectral range of the camera. The setup covered a field of view (FOV) of 160 mm \times 153 mm with a maximum resolution of 640 pixels \times 512 pixels. Increasing attenuation of the impinging radiation occurred toward the outer bounds of the FOV due to atmospheric attenuation and the clear aperture of the viewing window. The correction of this vignetting effect is beyond the scope of this study. For this reason, the effective FOV was reduced to 384 pixels \times 312 pixels. The size of this area was evaluated by viewing a black body plate at a constant temperature of 353 K. The frame rate was set to 1620.67 Hz. The integration time of the camera was set to 0.0103 ms in accordance with the calibration of the manufacturer.

Experimental Setup

To investigate the effect of the build height on the cooling rate and the resulting material properties of the 316L specimens, cubical towers of the dimension 10 mm \times 10 mm \times 150 mm were manufactured. Gas-atomized 316L stainless steel powder (OC Oerlikon Corporation, Pfäeffikon, Switzerland) with a particle size distribution of 19 to 46 μm was used for this purpose. Two towers were placed on the build platform within the FOV of the thermographic camera. To prevent any mutual thermal influencing, the distance between the towers was set to 48 mm.

The laser power was 190 W, the scanning speed was 800 mm/s, and the hatch distance was 100 μm . A single post-exposure of the contours was applied with a laser power of 190 W and a scanning speed of 800 mm/s. The specimens were built by applying a unidirectional scanning strategy with a rotation of 90° per layer. The scan vectors were parallel to the edge of the specimens, resulting in a constant scan vector length of 10 mm. The parts and the scanning pattern were rotated by 30° around the Z axis to prevent exposure toward the shielding gas flow. A second set of two towers was manufactured in a subsequent build job to investigate any potential differences between build jobs. After manufacturing, the towers were cut from the build plate using a band saw. No additional heat treatment was applied when testing the as-built properties of the specimens. The cooling rate was measured every 1 mm for the first 15 mm of the build height, every 5 mm thereafter up to 30 mm, and every 10 mm for the remainder of the build.

Post-process Analysis

The two towers from each build job were analyzed to determine their local material properties, as illustrated in Fig. 3. The specimens were sectioned with an abrasive cutting

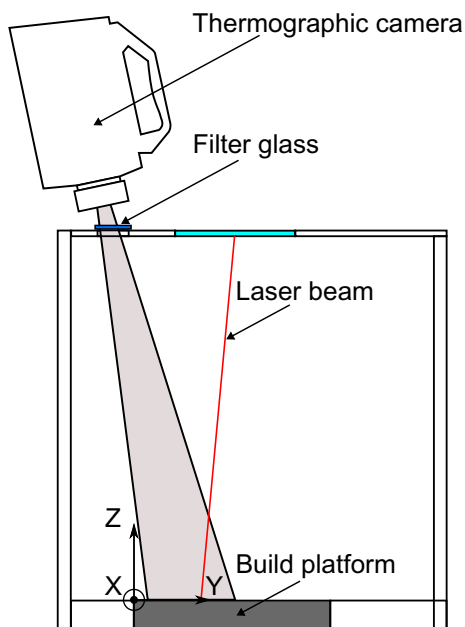


Fig. 2 Thermographic setup employed in this study; a high-speed thermographic camera was mounted on the top of the build chamber of the PBF-LB/M machine

machine QCut 100 (ATM Qness, Golling an der Salzach, Salzburg, Austria). One tower from each build job was cut centrally along the X-Z plane and each half was divided into sections of a height of 25 mm. The second tower from each build job was sectioned along the X-Y plane every 10 mm. The cross sections were then embedded, ground, and polished.

The Vickers hardness HV 1 of each cross section was tested at several points over the surface. The transversal cross sections were tested in a 3 × 3 matrix pattern, with a distance of 4 mm between the indentations and a clearance of 1 mm to the edges. The longitudinal cross sections were tested every 10 mm in the Z-direction with three centered indentations per Z-height at a distance of 1 mm to each other. A Qness 60A+ EVO microhardness tester (ATM Qness, Golling an der Salzach, Salzburg, Austria) was used for this purpose.

Correlation of Cooling Rate and Hardness

The intergranular cell structure is the primary strengthening mechanism in PBF-LB/M fabricated 316L [20]. The cooling rates during the process influence the cell size of this sub-grain structure. For fully austenitic stainless steels, the relationship between the cell size d_c and the cooling rate is expressed by [21]

$$d_c = 80 \cdot \dot{T}^{-0.33}. \quad (6)$$

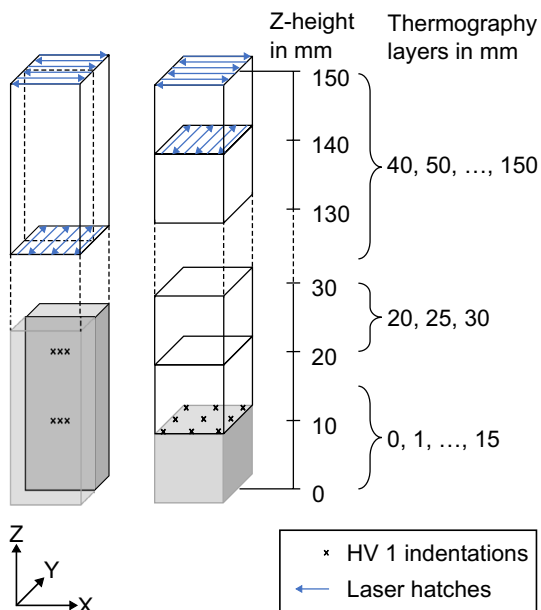


Fig. 3 Schematic of the tower specimens showing the section planes for the post-process analysis

With grain refinement, a higher stress is needed for a dislocation movement between the grains. The Hall–Petch relationship describes this correlation [22]:

$$\sigma_y = \sigma_0 + k \cdot d_g^{-0.5} \quad (7)$$

Here, σ_0 is the maximum yield stress needed for a dislocation of a single crystal, d_g is the grain size, and k is a constant describing the grain boundary resistance. Wang et al. [23] showed that the microhardness of 316L manufactured by PBF-LB/M correlates well with the cell size using a Hall–Petch type relationship by replacing the stress with the hardness and the grain size with the cell size d_c . This leads to a modified version of Eq. (7):

$$HV_y = HV_0 + k \cdot d_c^{-0.5} \quad (8)$$

The above relationships can be used to correlate the cooling rate to the hardness. The mean cell size is estimated by Eq. (6) using the mean cooling rate measured for the layer. A Hall–Petch type curve, Eq. (8), is fitted using the estimated mean cell size and the mean hardness of each layer, to demonstrate the validity of the measured cooling rates.

Results and Discussion

Solidification Point Detection

The camera intensity value at the solidification temperature was evaluated for all monitored layers. The values of the pixels in each single layer had a normal distribution. The mean value of the intensity increased from layer to layer, even though the temperature of the solidification transition is a material-specific constant. This offset was induced by the increasing surface temperature due to heat accumulation in the part. The camera value of a pixel was affected by the temperature of its surroundings. The surface temperature of the part thus contributed to the signal value of the melt pool pixel. A higher thermographic resolution would reduce this offset. However, the effect was compensated for by evaluating the camera value corresponding to the solidification temperature for each layer. The median value of each layer was used for the subsequent calculation of the cooling rate.

Cooling Rate

Figure 4 shows the temperature profile of a pixel at 140 mm build height. After the single-point temperature correction of T_{app} , the cooling curve was extracted from T_{true} and the temperature model, Eq. (3), was fitted to the extracted data. The

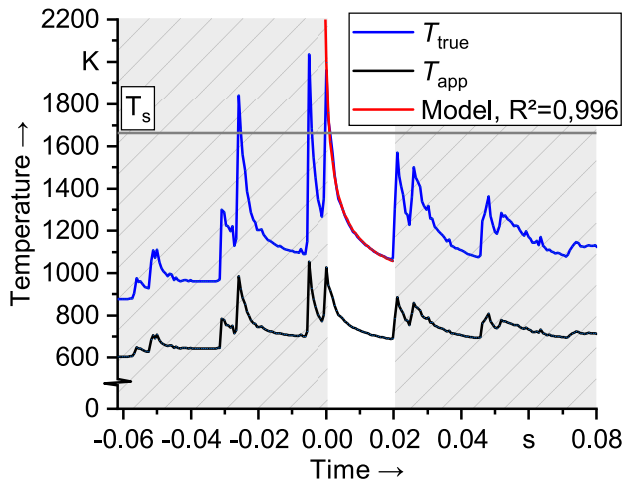


Fig. 4 Temperature profile of a pixel at 140 mm build height; the measured data T_{app} (black) was corrected for T_s (gray line) using ϵ_{app} ; the extracted cooling curve (white background) was fitted with the temperature model (red) proposed by [19]

model fitted well to the measurement data. In the example of the pixel data shown in Fig. 4, an $R^2 = 0.996$ was reached. Overall, 99% of all fittings reached an $R^2 \geq 0.974$. Note that, as described above, fittings with an $R^2 < 0.95$ were rejected.

Figure 5 shows the evaluated mean cooling rates of the different layers during the build of the four towers. The cooling rate curves of the towers displayed similar progressions. The maximum relative standard error of the various means was 1.58%. This shows the high reproducibility of the cooling rate measurement methodology presented in this study. It also shows that the cooling rate during manufacturing is reproducible for the same geometry at different locations on the build platform and for individual build jobs.

The cooling rate decreased significantly with increasing build height (see Fig. 5). The mean cooling rate measured at a build height of 1 mm was 3.72×10^5 K/s. Up to a build height of 50 mm, the cooling rate decreased by 35% to 2.42×10^5 K/s. At a height of 140 mm, it had a value of 1.96×10^5 K/s, a reduction of 47% of the initial cooling rate near the build plate. The error bars in Fig. 5 show the standard deviation of the cooling rate of each layer. The deviation included measurement uncertainties, data processing errors, and actual variations of the cooling rate. The cooling rate changed within a single layer leading to standard deviations of about 20–30%. The small standard errors of the measurements indicate that the deviations within a single layer were mainly attributable to the scan pattern [10]. The cooling rate is lower at the turning point of the laser, since the laser remains in the same area for longer [7].

The decrease in the cooling rate over the height is due to a heat accumulation in the towers. An increasing temperature

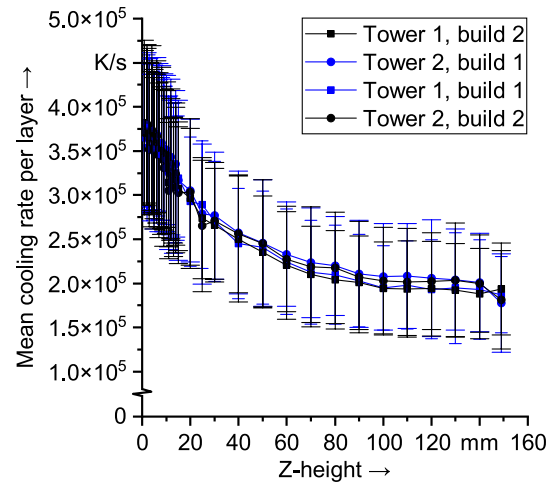


Fig. 5 The mean cooling rate and the standard deviation per layer; the cooling rate decreased with increasing build height; the progression of the cooling rate was reproducible between the different towers and build jobs

in the part leads to a lower temperature gradient between the melt pool and the topmost layers of the part. The level of the heat accumulation is dependent on the ILT. Shortening the ILT increases the surface temperature. Heat accumulation can be avoided if there is sufficient time for cooling between the layers [24, 25]. In the present study, the ILT of 14 s was comparably short, since only a small area of each layer was scanned.

Mechanical Properties

Figure 6 shows the hardness in the X-Y plane of the parts. The hardness decreased significantly with increasing height from 228 ± 9 HV 1 at 10 mm to 214 ± 5 HV 1 at 140 mm

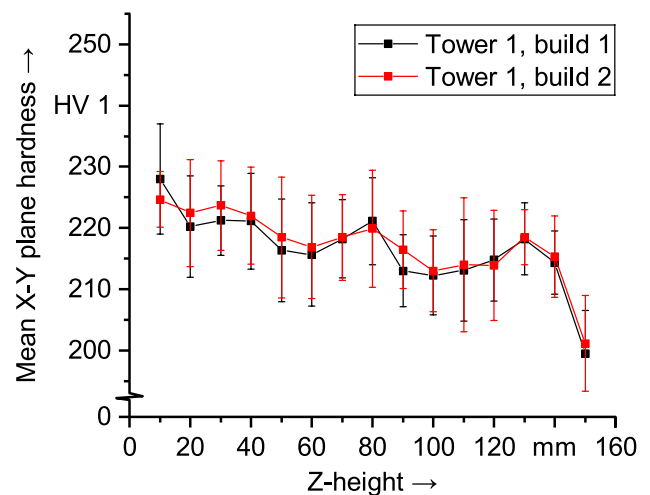


Fig. 6 The hardness values measured from transversal cross sections (X-Y plane) decrease significantly with the build height Z

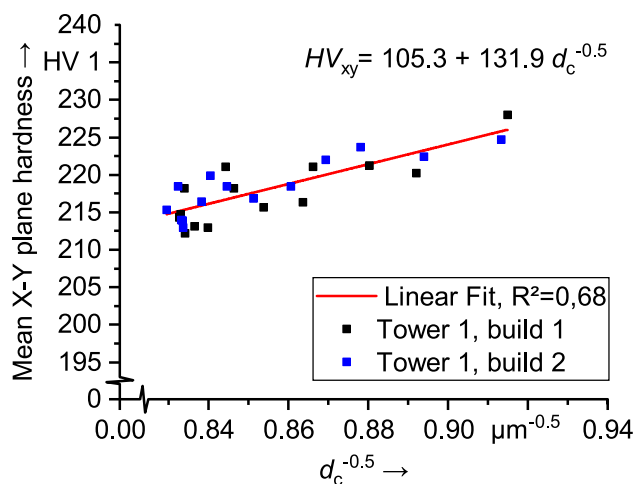


Fig. 7 Hall–Petch type relationship between the HV 1 hardness measured perpendicular to the building direction and the reciprocal square root of the cell size calculated from the cooling rate measurements

(ANOVA p value = 3.59×10^{-8}). The value of the top of the towers at about 150 mm was lower, at 199 ± 7 HV 1.

The hardness profiles for the X-Y planes of the two towers did not differ significantly between both samples (ANOVA p value=0.44). This shows the reproducibility of local mechanical properties of similar parts between two build jobs. The hardness profile in the X-Z plane also showed a decreasing trend, with 243 ± 11 HV 1 at 10 mm and 221 ± 20 HV 1 at 140 mm (ANOVA p value= 6.85×10^{-4}). The hardness values in the X-Z plane were slightly higher than in the X-Y plane, indicating an anisotropy of the HV 1 hardness. The results of the hardness measurements are in line with those obtained by Waqar et al. [26]. The authors attributed the anisotropy to the multiple remelting of the individual layers [26].

Correlation of Cooling Rate and Hardness

The cell size was calculated from the measured cooling rates and correlated with the hardness measurements using a Hall–Petch type relationship. The hardness values of the top plane were excluded from this analysis, since they were influenced by the upskin process parameter set. This parameter set had a higher energy input than the infill parameters. A higher energy input results in lower cooling rates [6], which explains the low hardness values at the top plane. The results are shown in Fig. 7.

The linear fitting of the Hall–Petch relationship between the calculated cell sizes and the hardness in the X-Y plane had a coefficient of determination of $R^2 = 0.68$. The correlation showed that it is generally possible to identify local variations in microstructure and mechanical properties by the cooling rate measurement methodology proposed in this work. However, a prediction of the mechanical properties is

not possible since the correlation presented here is based on mean values determined for each layer.

Conclusions

This paper describes a methodology for measuring cooling rates during the PBF-LB/M process. A five-step data evaluation procedure was used to evaluate the cooling rates from in situ thermographic measurements. The methodology was tested using a large FOV thermographic setup mounted on an EOS M280. The setup enabled the observation of an area of $96 \text{ mm} \times 78 \text{ mm}$ with a spatial resolution of $250 \text{ } \mu\text{m}/\text{pixel}$. To evaluate the reproducibility, four cubical towers of the dimensions $10 \text{ mm} \times 10 \text{ mm} \times 150 \text{ mm}$ were manufactured in two build jobs. The cooling rates were measured in several layers along the build height. The HV 1 microhardness profile was tested along the build height, perpendicularly and parallel to the building direction. The cooling rates and the mechanical properties of the parts were correlated using a Hall–Petch type relationship. The following conclusions can be drawn from the findings of this work:

- The cooling rate measurements for a thermographic setup with a large FOV showed reproducible results both for different locations on the build platform and for different build jobs. The maximum standard error of the mean of all four test specimens was 1.58%.
- The mean cooling rate per layer decreased by 47% from $3.72 \times 10^5 \text{ K/s}$ at a build height of 1 mm to $1.96 \times 10^5 \text{ K/s}$ at a build height of 140 mm.
- The mean hardness decreased significantly from 228 ± 9 HV 1 at 10 mm to 214 ± 5 HV 1 at 140 mm, measured perpendicularly to the building direction and from 243 ± 11 HV 1 at 10 mm to 221 ± 20 HV 1 at 140 mm, measured parallel to the building direction.
- It was possible to correlate the measured cooling rate with the hardness of the test specimens. The cell size was first approximated by the cooling rates and then correlated to the hardness by a Hall–Petch type relationship with an R^2 of 0.68.

The present analysis focused on the mean cooling rate per layer. Future work will focus on the effect of the scanning strategy, measurement uncertainties, and data processing errors. The next step is to apply the methodology to more complex, large-scale parts. It will be necessary to analyze different areas within the same layer separately, with significant differences in the surface temperature.

Supplementary Information

The datasets generated during this study are available in the mediaTUM repository at <https://doi.org/10.14459/2023mp1695278>.

Appendix

Additional Figures

See Figs. 8, 9, 10, 11, and 12.

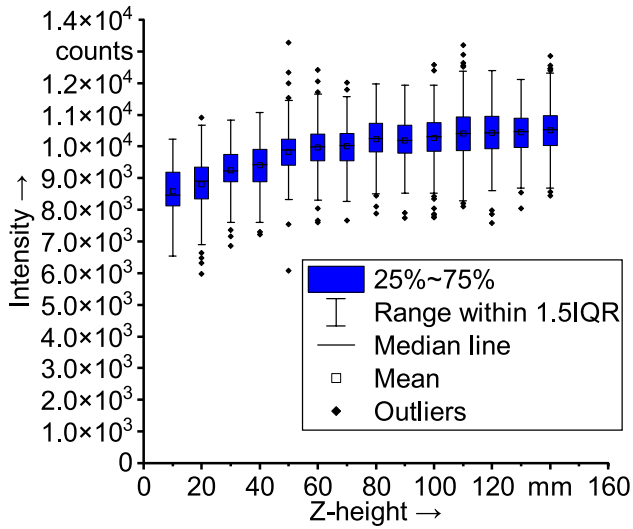


Fig. 8 Box plot of the camera intensity values of the solidification temperature (IQR: interquartile range); the values increase with the build height due to a signal offset induced by the increasing surrounding temperature

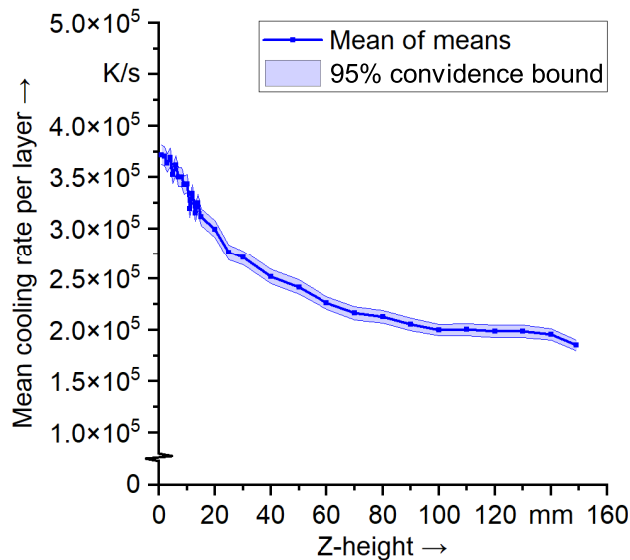


Fig. 9 The confidence interval of the cooling rate was calculated as 1.96 times the standard error of the mean of the four towers

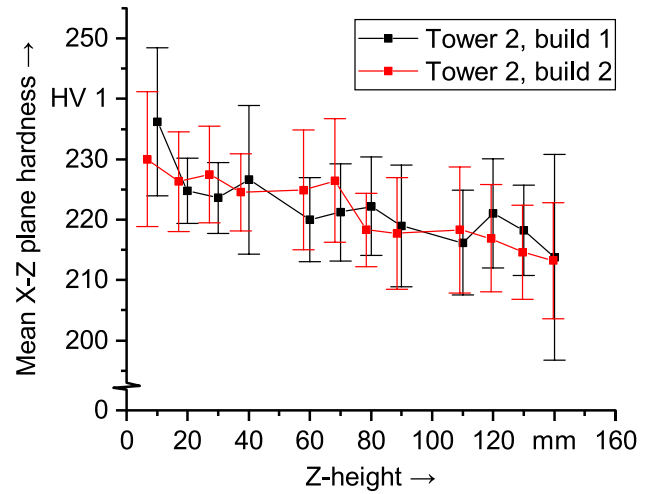


Fig. 10 The hardness values measured from longitudinal cross sections (X-Z plane) decrease significantly with the build height Z

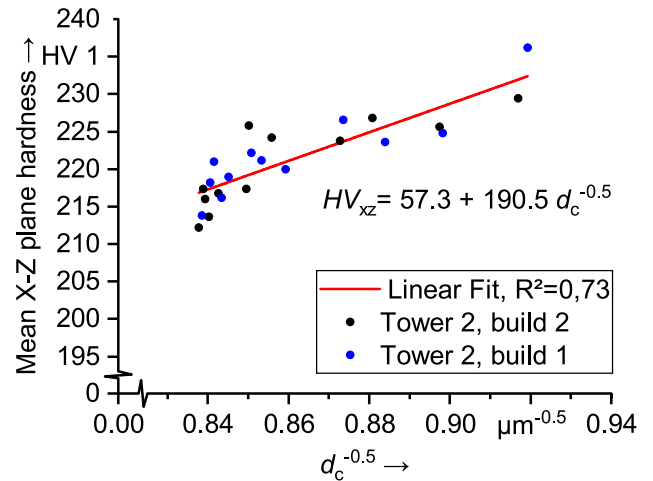


Fig. 11 Hall–Petch type relationship between the HV 1 hardness measured parallel to the building direction and the reciprocal square root of the cell size calculated from the cooling rate measurements

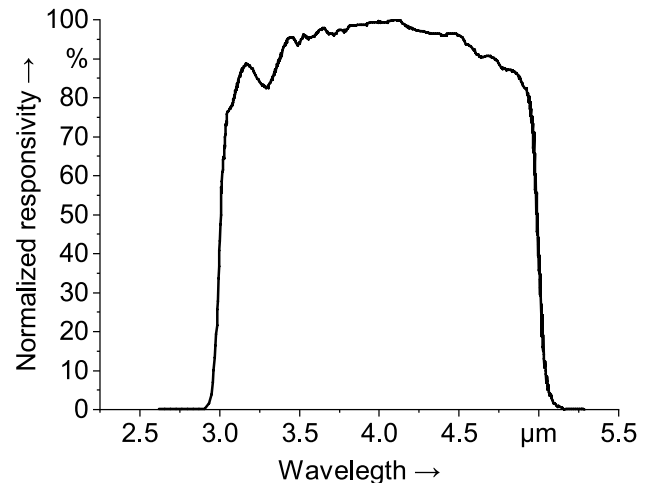


Fig. 12 Normalized responsivity of the sensor of the thermographic camera Flir xc6901sc [27]

Summary of the ANOVA Analysis Results

See Tables 1, 2 and 3.

Table 1 Summary of the ANOVA analysis for the X-Y hardness

	Degree of freedom	Sum of squares	Mean square	<i>F</i> value	<i>p</i> value
Height	13	3703.49	284.88	5.21	3.59×10^{-8}
Part	1	32.14	32.14	0.59	0.44
Error	237	12957.97	54.68		
Total	251	16693.60			

Table 2 Summary of the ANOVA analysis for the X-Z hardness

	Degree of freedom	Sum of squares	Mean square	<i>F</i> value	<i>p</i> value
Height	11	2148.82	195.35	3.57	6.85×10^{-4}
Part	1	30.68	30.68	0.56	0.46
Error	107	3224.49	54.65		
Total	119	5403.99			

Table 3 Summary of the ANOVA analysis for the hardness of the planes X-Y and X-Z

	Degree of freedom	Sum of squares	Mean square	<i>F</i> value	<i>p</i> value
Plane	1	3770.01	3770.04	91.72	1.27×10^{-13}
Height	11	1386.49	126.044	3.07	2.62×10^{-3}
Error	59	2425.15	41.10		
Total	71	7581.65			

For this analysis, only X-Y plane indentations at $Y = 5$ mm were used for comparability

Acknowledgements This research was funded by the Deutsche Forschungsgemeinschaft (DFG, German Research Foundation), project number 414265976–TRR 277.

Funding Open Access funding enabled and organized by Projekt DEAL.

Declarations

Conflict of interest The authors declare that they have no conflict of interest.

Open Access This article is licensed under a Creative Commons Attribution 4.0 International License, which permits use, sharing, adaptation, distribution and reproduction in any medium or format, as long

as you give appropriate credit to the original author(s) and the source, provide a link to the Creative Commons licence, and indicate if changes were made. The images or other third party material in this article are included in the article's Creative Commons licence, unless indicated otherwise in a credit line to the material. If material is not included in the article's Creative Commons licence and your intended use is not permitted by statutory regulation or exceeds the permitted use, you will need to obtain permission directly from the copyright holder. To view a copy of this licence, visit <http://creativecommons.org/licenses/by/4.0/>.

References

- Ghantasa A, Diller J, Geiser A, Wenzler LD, Siebert D, Radlbeck C et al (2021) Node-based shape optimization and mechanical test validation of complex metal components and support structures, manufactured by laser powder bed fusion. *Advances in manufacturing, production management and process control*, vol 274. Springer, Cham, pp 10–17
- Munk J, Breitbarth E, Siemer T, Pirch N, Häfner C (2022) Geometry effect on microstructure and mechanical properties in laser powder bed fusion of Ti-6Al-4V. *Metals*. <https://doi.org/10.3390/met12030482>
- Zhong Y, Liu L, Wikman S, Cui D, Shen Z (2016) Intragranular cellular segregation network structure strengthening 316L stainless steel prepared by selective laser melting. *J Nucl Mater* 470:170–178. <https://doi.org/10.1016/j.jnucmat.2015.12.034>
- Diller J, Auer U, Radlbeck C, Mensinger M, Krafft F (2020) Einfluss der Abkühlrate auf die mechanischen Eigenschaften von additiv gefertigten Zugproben aus 316L. *Stahlbau* 89:970–980. <https://doi.org/10.1002/stab.202000034>
- Raplee J, Plotkowski A, Kirka MM, Dinwiddie R, Okello A, Dehoff RR et al (2017) Thermographic microstructure monitoring in electron beam additive manufacturing. *Sci Rep*. <https://doi.org/10.1038/srep43554>
- Scipioni Bertoli U, Guss G, Wu S, Matthews JM, Schoenung MJ (2017) In-situ characterization of laser-powder interaction and cooling rates through high-speed imaging of powder bed fusion additive manufacturing. *Mater Des* 135:385–396. <https://doi.org/10.1016/j.matdes.2017.09.044>
- Evans R, Walker J, Middendorf J, Gockel J (2020) Modeling and monitoring of the effect of scan strategy on microstructure in additive manufacturing. *Metall Mater Trans A* 51(8):4123–4129. <https://doi.org/10.1007/s11661-020-05830-0>
- Plotkowski A, Kirka MM, Babu SS (2017) Verification and validation of a rapid heat transfer calculation methodology for transient melt pool solidification conditions in powder bed metal additive manufacturing. *Addit Manuf* 18:256–268. <https://doi.org/10.1016/j.addma.2017.10.017>
- Hooper AP (2018) Melt pool temperature and cooling rates in laser powder bed fusion. *Addit Manuf* 22:548–559. <https://doi.org/10.1016/j.addma.2018.05.032>
- Heigel CJ, Lane MB, Levine EL (2020) In situ measurements of melt-pool length and cooling rate during 3D builds of the metal AM-bench artifacts. *Integr Mater Manuf Innov* 9(1):31–53. <https://doi.org/10.1007/s40192-020-00170-8>
- Wimmer A, Hofstaetter F, Jugert C, Wudy K, Zaeh FM (2022) In situ alloying: investigation of the melt pool stability during powder bed fusion of metals using a laser beam in a novel experimental set-up. *Prog Addit Manuf* 7(2):351–359. <https://doi.org/10.1007/s40964-021-00233-y>
- Lane B, Whinton E, Madhavan V, Donmez A (2013) Uncertainty of temperature measurements by infrared thermography for metal cutting applications. *Metrologia* 50(6):637–653. <https://doi.org/10.1088/0026-1394/50/6/637>

13. Wimmer A, Kolb GC, Assi M, Favre J, Bachmann A, Fraczkiewicz A et al (2020) Investigations on the influence of adapted metal-based alloys on the process of laser beam melting. *J Laser Appl*. <https://doi.org/10.2351/7.0000071>
14. Heigel CJ, Lane MB (2018) Measurement of the melt pool length during single scan tracks in a commercial laser powder bed fusion process. *J Manuf Sci Eng*. <https://doi.org/10.1115/1.4037571>
15. Hunnewell ST, Walton LK, Sharma S, Ghosh KT, Tompson VR, Viswanath SD et al (2017) Total hemispherical emissivity of SS 316L with simulated very high temperature reactor surface conditions. *Nucl Technol* 198(3):293–305. <https://doi.org/10.1080/00295450.2017.1311120>
16. del Campo L, Pérez-Sáez BR, González-Fernández L, Esquisabel X, Fernández I, González-Martín P et al (2010) Emissivity measurements on aeronautical alloys. *J Alloys Compd* 489(2):482–487. <https://doi.org/10.1016/j.jallcom.2009.09.091>
17. Schmid S, Krabusch J, Schromm T, Jieqing S, Ziegelmeier S, Grosse UC et al (2021) A new approach for automated measuring of the melt pool geometry in laser-powder bed fusion. *Prog Addit Manuf* 6(2):269–279. <https://doi.org/10.1007/s40964-021-00173-7>
18. Leicht A, Fischer M, Klement U, Nyborg L, Hryha E (2021) Increasing the productivity of laser powder bed fusion for stainless steel 316L through increased layer thickness. *J Mater Eng Perform* 30(1):575–584. <https://doi.org/10.1007/s11665-020-05334-3>
19. Krauss H, Zeugner T, Zaeh FM (2014) Layerwise monitoring of the selective laser melting process by thermography. *Phys Procedia* 56:64–71. <https://doi.org/10.1016/j.phpro.2014.08.097>
20. Riabov D, Leicht A, Ahlström J, Hryha E (2021) Investigation of the strengthening mechanism in 316L stainless steel produced with laser powder bed fusion. *Mater Sci Eng A*. <https://doi.org/10.1016/j.msea.2021.141699>
21. Katayama S, Matsunawa A (1984) Solidification microstructure of laser welded stainless steels. In: *International congress on applications of lasers & electro-optics*. Laser Institute of America. p 60–67
22. Kashyap PB, Tangri K (1995) On the hall-petch relationship and substructural evolution in type 316L stainless steel. *Acta Metall et Mater* 43(11):3971–3981. [https://doi.org/10.1016/0956-7151\(95\)00110-H](https://doi.org/10.1016/0956-7151(95)00110-H)
23. Wang X, Muñoz-Lerma AJ, Sánchez-Mata O, Attarian Shandiz M, Brochu M (2018) Microstructure and mechanical properties of stainless steel 316L vertical struts manufactured by laser powder bed fusion process. *Mater Sci Eng A* 736:27–40. <https://doi.org/10.1016/j.msea.2018.08.069>
24. Williams JR, Piglione A, Rønneberg T, Jones C, Pham M, Davies MC et al (2019) In situ thermography for laser powder bed fusion: effects of layer temperature on porosity, microstructure and mechanical properties. *Addit Manuf*. <https://doi.org/10.1016/j.addma.2019.100880>
25. Mohr G, Altenburg JS, Hilgenberg K (2020) Effects of inter layer time and build height on resulting properties of 316L stainless steel processed by laser powder bed fusion. *Addit Manuf*. <https://doi.org/10.1016/j.addma.2020.101080>
26. Waqar S, Liu J, Sun Q, Guo K, Sun J (2020) Effect of post-heat treatment cooling on microstructure and mechanical properties of selective laser melting manufactured austenitic 316L stainless steel. *Rapid Prototyp J* 26(10):1739–1749. <https://doi.org/10.1108/RPJ-12-2019-0320>
27. FLIR Systems (2020) Spectral response curves of various photonic sensors. https://flir.custhelp.com/app/answers/detail/a_id/3634/~spectral-response-curves-of-various-photonic-sensors

Publisher's Note Springer Nature remains neutral with regard to jurisdictional claims in published maps and institutional affiliations.